Applied Catalysis B: Environmental 111–112 (2012) 280–287

Contents lists available at SciVerse ScienceDirect

Applied Catalysis B: Environmental

journal homepage: www.elsevier.com/locate/apcatb

Combination of cobalt ferrite and graphene: High-performance and recyclable visible-light photocatalysis

Yongsheng Fu[a,b], Haiqun Chen[b,**], Xiaoqiang Sun[b], Xin Wang[a,c,*]

[a] Key Laboratory of Soft Chemistry and Functional Materials, Nanjing University of Science and Technology, Ministry of Education, Nanjing 210094, China
[b] Key Laboratory of Fine Petrochemical Engineering, Changzhou University, Changzhou 213164, China
[c] Key Laboratory of Jiangsu Province for Chemical Pollution Control and Resources Reuse, Nanjing University of Science and Technology, Nanjing 210094, China

ARTICLE INFO

Article history:
Received 9 July 2011
Received in revised form
30 September 2011
Accepted 4 October 2011
Available online 12 October 2011

Keywords:
Cobalt ferrite
Graphene
Photocatalyst
Magnetic separation
Visible-light irradiation

ABSTRACT

A straightforward strategy was designed for the fabrication of magnetically separable $CoFe_2O_4$-graphene photocatalysts with differing graphene content. It is very interesting that the combination of $CoFe_2O_4$ nanoparticles with graphene results in a dramatic conversion of the inert $CoFe_2O_4$ into a highly active catalyst for the degradation of methylene blue (MB), Rhodamine B (RhB), methyl orange (MO), active black BL-G and active red RGB under visible-light irradiation. The significant enhancement in photoactivity under visible-light irradiation can be ascribed to reduction of graphene oxide, because the photogenerated electrons of $CoFe_2O_4$ can transfer easily from the conduction band to the reduced graphene oxide, effectively preventing a direct recombination of electrons and holes. Hydroxyl radicals play the role of main oxidant in the $CoFe_2O_4$-graphene system and the radicals' oxidation reaction is obviously dominant. $CoFe_2O_4$ nanoparticles themselves have a strong magnetic property, which can be used for magnetic separation in a suspension system, and therefore the introduction of additional magnetic supports is no longer necessary.

1. Introduction

Graphene, the two-dimensional (2D) crystal of hybridized carbon, has become a major research topic in physical, chemical and materials sciences in recent years and has many potential applications [1–5]. Because of its large specific surface area, remarkable electrical conductivity, excellent adsorptivity, and high chemical and thermal stability, graphene has been receiving recent attention as a support for catalysts [6–8]. Some efforts have been made to utilize UV irradiation with graphene–metal oxide composites [9–15]. However, so far, relatively little attention has been paid to graphene-based visible-light-driven photocatalysts [16,17].

Magnetic nanoparticles are subject to intense research, because they possess attractive properties which could see potential use in catalysis, biomedicine and environmental remediation [18–21]. Among the magnetic nanoparticles, nanosized cobalt ferrite ($CoFe_2O_4$) particles are occupying an important place for their unusual properties such as magnetocrystalline anisotropy, high coercivity and moderate saturation magnetization [22]. A $CoFe_2O_4$ nanocatalyst (40–50 nm) was used as an efficient quasi-homogenous catalyst for a Knoevenagel condensation reaction of several aldehydes with ethylcyanoacetate and could be recovered from the reaction mixture by compartmentation with the aid of an external magnet [23]. Magnetic $CoFe_2O_4$ nanoparticles have been used to fabricate titania-coated cobalt ferrite, allowing easy separation of the photocatalysts after the oxidative process [24].It has been found that there are concerted effects of the individual components in graphene-based nanocomposites [6]. To understand the nature of synergistic effects between $CoFe_2O_4$ magnetic nanoparticles and graphene, some studies have been conducted, including studies of the adsorption properties of $CoFe_2O_4$ nanoparticles (10–40 nm) supported on graphene sheets and the interaction of $CoFe_2O_4$ with graphene [25,26]. Obviously, in such a composite, $CoFe_2O_4$ nanocrystals with smaller particle size (<10 nm) will give rise to higher surface area and other improved properties.

Recently we reported a magnetically separable $ZnFe_2O_4$-graphene photocatalyst with different graphene content, and its high performance in the photocatalytic degradation of methylene blue (MB) in the presence of hydrogen peroxide under visible-light irradiation [17]. However, hydrogen peroxide is manufactured by a process that consumes energy and/or other chemical resources. It is of great interest to design magnetically separable graphene-based photocatalysts having high catalytic activity without using

* Corresponding author at: Key Laboratory of Soft Chemistry and Functional Materials, Nanjing University of Science and Technology, Ministry of Education, Nanjing 210094, China. Tel.: +86 25 8431 5943; fax: +86 25 8431 5054.
** Corresponding author.
E-mail addresses: chenhq@cczu.edu.cn (H. Chen), wxin@public1.ptt.js.cn (X. Wang).

0926-3373/$ – see front matter © 2011 Elsevier B.V. All rights reserved.
doi:10.1016/j.apcatb.2011.10.009

hydrogen peroxide. If that can be accomplished, then it should be possible to obtain much more effective and green photocatalysts.

Herein, we demonstrate a simple and straightforward strategy to fabricate a $CoFe_2O_4$-graphene nanocomposite via a one-step hydrothermal method. In the as-obtained composite, $CoFe_2O_4$ nanocrystals have an average diameter of 5.53 nm and a narrow particle size distribution. It is interesting that although $CoFe_2O_4$ alone is photocatalytically inactive under visible-light irradiation, the combination of $CoFe_2O_4$ and graphene leads to high photocatalytic activity for the degradation of MB under visible-light irradiation. The excellent magnetic properties of $CoFe_2O_4$ were maintained in the composite, and therefore the photocatalyst could be separated easily by an external magnetic field.

2. Experimental

2.1. Synthesis of magnetic $CoFe_2O_4$-graphene composite photocatalyst

Graphite oxide (GO) was synthesized from purified natural graphite bought from Shanghai Yifan Company with a mean particle size of 1.5 μm according to the method reported by Hummers and Offeman [27]. $CoFe_2O_4$-graphene nanocomposite photocatalysts with differing graphene content (15, 20, 25, 30, 35, 40, 50 wt%) were synthesized according to ref. [17]. A typical experiment for the synthesis of $CoFe_2O_4$-graphene nanocomposite with 40% graphene content is as follows: 80 mg of GO was dispersed into 60 mL of absolute ethanol with sonication for 1 h. Then 0.1486 g of $Co(NO_3)_2{\cdot}6H_2O$ and 0.4126 g of $Fe(NO_3)_3{\cdot}9H_2O$ were added to 20 mL of absolute ethanol with stirring for 30 min at room temperature. The above two systems were then mixed together, and stirred for 30 min. Then the reaction mixture was adjusted to a pH of 10.0 with 6 M NaOH solution, and stirred for 30 min, yielding a stable bottle-green homogeneous emulsion. The resulting mixture was transferred into a 100 mL Teflon-lined stainless steel autoclave and heated to 180 °C for 20 h under autogenous pressure. The reaction mixture was allowed to cool to room temperature and the precipitate was filtered, washed with distilled water five times, and dried in a vacuum oven at 60 °C for 12 h. The product was labeled as $CoFe_2O_4$-G(0.4). For comparison, same method was used to synthesize pure $CoFe_2O_4$ without GO.

2.2. Characterization

Fourier transform infrared (FTIR) spectra were recorded on a Bruker VECTOR 22 spectrometer using the KBr pellet technique. X-ray photoelectron spectra (XPS) were carried out on a RBD upgraded PHI-5000C ESCA system (Perkin Elmer) with Mg Kα radiation ($h\nu$ = 1253.6 eV). Raman spectra were acquired on a Renishaw inVia Reflex Raman Microprobe. Powder X-ray diffraction (XRD) analyses were performed on a Bruker D8 Advanced diffractometer with Cu Kα radiation and the scanning angle ranged from 5° to 70° of 2θ. Transmission electron microscopy (TEM) images were taken with a JEOL JEM2100 microscope. Photoluminescence spectra were recorded on a Jobin Yvon SPEX Fluorolog-3-P spectroscope and a 450 W Xe lamp was used as the excitation source. Nitrogen adsorption–desorption isotherms were measured at 77 K on a Micromeritics Model TriStar II 3020 volumetric analyzer.

Electrochemical impedance spectroscopy (EIS) measurements were performed with a CHI660B workstation. The test electrodes were prepared according to ref. [28]. EIS measurements were carried out in 1 M H_2SO_4 by using a three-electrode system, with a platinum foil electrode as the counter electrode and a saturated calomel electrode (SCE) as the reference electrode. EIS measurements were recorded with an AC voltage amplitude of 5 mV, with a frequency range of 1 MHz to 5 mHz at 0.5 V.

2.3. Photocatalytic activity measurement

The photocatalytic activity of the prepared samples was determined by the degradation of MB, Rhodamine B (RhB), methyl orange (MO), active black BL-G and active red RGB under visible-light irradiation. Photo-irradiation was carried out using a 500 W xenon lamp through UV cut-off filters (JB450) to completely remove any radiation below 420 nm and to ensure illumination by visible-light only. Experiments were conducted at 25 °C in the following manner: take MB for instance, 0.025 g of photocatalyst was added to 100 mL of a 20 mg/L dye aqueous solution. Before starting the illumination, the reaction mixture was stirred for 120 min in the dark in order to reach the adsorption–desorption equilibrium between the dye and the catalyst. At given time intervals of irradiation, 5 mL aliquots were withdrawn, and then magnetically separated to remove essentially all the catalyst. The concentrations of the remnant dye were spectrophotometrically monitored by measuring the absorbance of solutions at 664 nm during the photodegradation process. After photocatalytic reactions on the $CoFe_2O_4$-G(0.4) system, the aqueous solution was analyzed using ion chromatography system (Dionex ICS-90).

Photocurrent was measured on a CHI 660B electrochemical workstation in a standard three-electrode system using the prepared samples as the working electrodes with an active area of ca. 0.5 cm^2. Platinum foil and an SCE were used as the counter and reference electrodes, respectively. A 500 W xenon lamp with a 420 nm cut-off filter (the average light intensity was 31.2 mW cm^{-2}) was used as the source of visible-light irradiation.

2.4. Adsorption kinetic studies

The adsorption kinetic studies of MB over $CoFe_2O_4$-G(0.4) were carried out in the dark, and 2 h was chosen as the adsorption equilibrium time. A batch of equilibrium adsorption experiments were conducted in the dark at 20 °C.A range of initial concentrations (10, 20, 30, 40, 50, 60, 80, 100, 200, 300 mg/L) with a fixed weight (0.01 g/30 mL) of the $CoFe_2O_4$-G(0.4) samples were chosen to obtain the adsorption isotherms of MB over $CoFe_2O_4$-G(0.4). After reaching equilibrium, the mixture was magnetically separated to remove essentially all the catalyst. The absorbance of the MB at 664 nm was measured to determine the equilibrium concentration. The amount of adsorbed MB per gram $CoFe_2O_4$-G(0.4) at equilibrium, q_e (mg/g), was obtained by

$$k = \frac{1}{t} \ln \frac{c}{c_0} \quad (1)$$

where c_0 and c_e (mg/L) are the initial and equilibrium concentration of MB, respectively. V (L) is the volume of the solution, and W (g) is the weight of $CoFe_2O_4$-G(0.4) used.

3. Results and discussion

3.1. Structure and morphology of $CoFe_2O_4$-graphene nanocomposite photocatalyst

The morphology of as-obtained $CoFe_2O_4$-graphene nanocomposite investigated by TEM is shown in Fig. 1A and B. The almost transparent graphene sheets are fully exfoliated and decorated with $CoFe_2O_4$ nanocrystals having an average diameter of 5.53 nm and a narrow particle size distribution (Fig. 1C). $CoFe_2O_4$ nanocrystals anchored on the surface of graphene sheets have a good dispersion property and larger surface area, which is expected to offer an enhanced photocatalytic activity. Previous studies

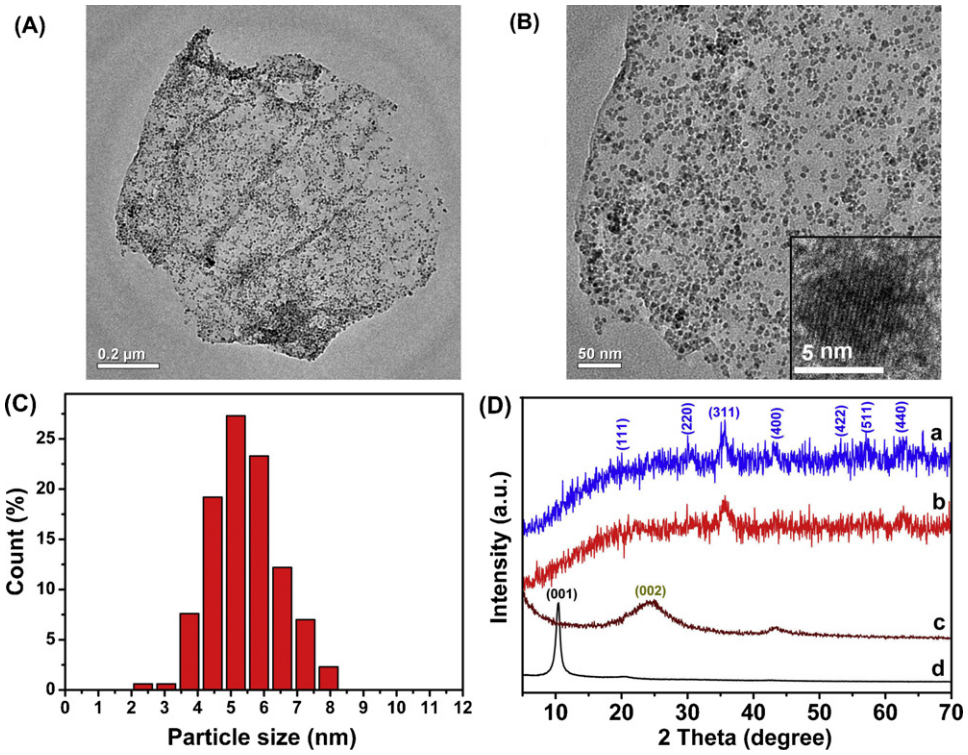

Fig. 1. (A) and (B) Typical TEM images of $CoFe_2O_4$-G(0.4); (C) the particle size distribution for $CoFe_2O_4$; (D) XRD patterns of (a) $CoFe_2O_4$-G(0.4), (b) pure $CoFe_2O_4$, (c) reduced graphene oxide and (d) graphite oxide (GO) in the range of 5–70°.

have shown the formation mechanism of graphene–metal oxide nanocomposites [6,29]. The oxygen-containing functional groups (COOH, C–OH, C–O–C) on the graphene oxide sheets can adsorb the positive cobalt and iron ions through electrostatic attraction. Then, graphene oxide sheets were converted to graphene sheets via solvothermal reduction [30,31], and the in situ formed $CoFe_2O_4$ nanocrystals were anchored on these graphene-based sheets, forming $CoFe_2O_4$-graphene hybrid composite. These in situ formed $CoFe_2O_4$ nanocrystals in return caused the exfoliation of the lamellar graphene, leading to the formation of the monolayer graphene. A dilute suspension of $CoFe_2O_4$-graphene was deposited onto a mica substrate and analyzed through atomic force microscopy (AFM). As shown in Fig. 1S (supporting information), the individual graphene sheets are decorated with $CoFe_2O_4$ nanoparticles. The cross section analysis shows a background height of 0.7 nm which corresponds to the thickness of the reduced graphene oxide sheet [32]. The peaks seen in this analysis (smaller peaks having a height of 3–8 nm) correspond to the $CoFe_2O_4$ nanoparticles (~4–7 nm in size) anchored on the graphene sheet. The AFM result is in good agreement with the TEM result. Fig. 2S (supporting information) gives the nitrogen adsorption isotherm of $CoFe_2O_4$-G(0.4). The isotherm shows a typical IUPAC type IV pattern, revealing the existence of mesopores. The measurements indicate that the sample has a Brunauer–Emmett–Teller (BET, nitrogen, 77 K) surface area of 259.97 $m^2\,g^{-1}$, with a pore volume of 0.096 $m^2\,g^{-1}$, and a BJH desorption average pore diameter of 3.20 nm. It is well known that the mesoporous structure is a more efficient photocatalyst structure for degradating organic pollutants in water.

The XRD diffraction patterns of the as-prepared $CoFe_2O_4$-graphene nanocomposites, pure $CoFe_2O_4$, reduced graphene oxide and graphite oxide (GO) are shown in Fig. 1D. It can be seen that almost all the diffraction peaks of $CoFe_2O_4$-graphene may be assigned to spinel-type $CoFe_2O_4$ (JCPDS 22-1086) [25]. However, no typical diffraction peak of graphite (0 0 2) or GO (0 0 1) is observable in the XRD pattern for $CoFe_2O_4$-graphene. This may be ascribed to the fact that during the hydrothermal reaction, crystal growth of $CoFe_2O_4$ between the interlayer of GO destroyed the regular layer stacking, leading to the exfoliation of GO and the disappearance of the (0 0 1) diffraction peak. On the other hand, graphene oxide sheets can be reduced under the hydrothermal conditions in the presence of alcohols, and the exfoliated reduced graphene oxide sheets show no peak of (0 0 2) [17]. As shown in Fig. 3S (supporting information), the intensity of diffraction peaks for the composites varies inversely with the graphene content.

Raman spectroscopy is also one of the most sensitive and informative techniques to characterize disorder in sp^2 carbon materials. As shown in Fig. 2A, for $CoFe_2O_4$-G(0.4), Raman peaks of G- and D-bands shift to lower frequency in comparison with that of GO: the G-band shifted from 1602 to 1589 cm^{-1}, whereas the D-band shifted from 1360 to 1347 cm^{-1}, indicating that GO has been reduced to graphene [33,34]. Additionally, the 2D band at 2696 cm^{-1} is also observed, which is further indicative of the reduction of GO and the formation of graphene. The peak position of the 2D band is similar to that of monolayer graphene [35–38]. The two Raman spectra of $CoFe_2O_4$-G(0.4) and pure $CoFe_2O_4$ show similar features in the range of 100–1000 cm^{-1}, and this is in agreement with published work on $CoFe_2O_4$ particles [39,40]. Fig. 4S (supporting information) shows the Raman spectra of the $CoFe_2O_4$-graphene nanocomposites with different graphene content. It is obvious that the intensity ratio of the D- to G-band ($I_{D\text{-band}}/I_{G\text{-band}}$) decreases with increasing graphene content in the $CoFe_2O_4$-graphene nanocomposites, indicative of the increase of degree of graphitization and the existence of graphene in the $CoFe_2O_4$-graphene nanocomposites.

Graphene can be obtained through various physical and chemical routes, including the removal of the oxygen from graphene oxide sheets via hydrothermal reaction in the presence of reducing agents [9,12]. The XPS results indicated a decrease of oxygen content in $CoFe_2O_4$-G(0.4) compared with that of GO (Table 1S, supporting information). As shown in Fig. 2B, the intensity of some

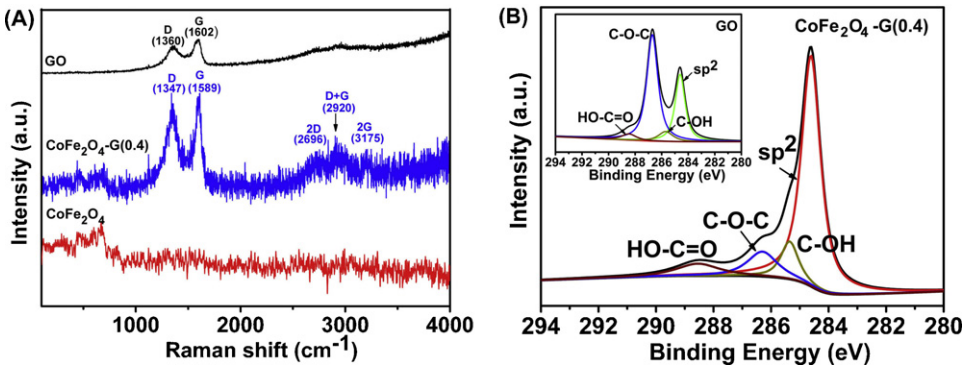

Fig. 2. (A) Raman spectra of GO, $CoFe_2O_4$-G(0.4) and pure $CoFe_2O_4$; (B) C 1s XPS spectra of $CoFe_2O_4$-G(0.4). The inset is C 1s XPS spectra of GO.

oxygen-containing groups on carbon sheets in the as-prepared composite was obviously reduced, indicating the deoxygenation of graphene oxide. Among the oxygen-containing groups on the carbon sheets, the epoxy groups were largely reduced in the composite compared with the starting GO. This shows that via hydrothermal reaction graphene oxide has been reduced to graphene with a tiny amount of residual oxygen-containing groups. Fig. 5S (supporting information) displays the typical Co 2p and Fe 2p XPS spectra of $CoFe_2O_4$-G(0.4), which is in agreement with published work on $CoFe_2O_4$ particles [41].

The UV–vis spectroscopy can be used to determine the change in the absorption of the samples and the results are shown in Fig. 6S. The UV–vis spectrum of graphene oxide exhibits an obvious characteristic absorption peak at about 230 nm, corresponding to π–π^* transition of aromatic C=C bonds. Compared with graphene oxide, the maximum absorption peak of reduced graphene oxide had a clear trend in red shift. For $CoFe_2O_4$-G(0.4), the typical absorption peak of graphene oxide at 230 nm disappears and the absorption band towards the visible light is broader compared to pure $CoFe_2O_4$, implying the $CoFe_2O_4$-G(0.4) hybrid composite can be used as photocatalyst under visible-light irradiation.

3.2. Photocatalytic properties and reaction kinetics

The photocatalytic activities of $CoFe_2O_4$-graphene and pure $CoFe_2O_4$ photocatalysts were evaluated by the degradation of dyes (MB, RhB, MO, active black BL-G and active red RGB) under visible-light irradiation.

The photodegradation rates of MB on the as-obtained $CoFe_2O_4$-graphene nanocomposite photocatalysts with differing graphene content and pure $CoFe_2O_4$ under visible-light irradiation at 25 °C are shown in Fig. 3A. The adsorption–desorption equilibrium solution of MB and $CoFe_2O_4$-G(0.4) was used as starting solution (t = 0 min). It is very interesting that $CoFe_2O_4$ or graphene is a photocatalytically inert compound (Fig. 3A(a and b)), whereas the hybrid of $CoFe_2O_4$ and graphene leads to dramatically enhancement of photocatalytic activity under visible-light irradiation (Fig. 3A(e–i)). With increasing graphene content in $CoFe_2O_4$-graphene photocatalyst, faster MB degradation was observed, and 40% (w/w) graphene in $CoFe_2O_4$-graphene gave the best performance in photocatalytic activity (Fig. 3A(h)). It can be clearly seen that almost all the MB molecules in the solution were decomposed after 240 min for the $CoFe_2O_4$-G(0.4).

Fig. 3B shows the photodegradation rates of RhB, MO, active black BL-G and active red RGB over $CoFe_2O_4$-G(0.4) under the same conditions as for MB. The photodegradation rates of RhB, MO, active black BL-G and active red RGB over $CoFe_2O_4$-G(0.4) reached 94, 71, 66 and 61% respectively after irradiation for 240 min, while the pure $CoFe_2O_4$ is a photocatalytically inert compound for these dyes under visible-light irradiation (data not shown).

It was demonstrated that the photocatalytic degradation of MB follows a pseudo-first-order kinetics behavior. The rate constant (k) can be calculated for the photocatalytic degradation of MB under visible-light irradiation at 25 °C according to Eq. (2).

$$q_e = \frac{(c_0 - c_e)V}{W} \quad (2)$$

where c_0 and c are the concentration of MB when reaction time is 0 and t, respectively. Fig. 3C shows the values for the pseudo-first-order rate constant (k) for the photodecomposition of MB by $CoFe_2O_4$-graphene photocatalysts with different graphene content. Among these catalysts, $CoFe_2O_4$-G(0.4) showed the highest rate constant of 0.01483 min^{-1}. In contrast, $CoFe_2O_4$-graphene with lower graphene content (<20%) gave a lower rate constant, and the photocatalytic activity of pure $CoFe_2O_4$ was negligible. The inset of Fig. 3C shows that the composite photocatalyst can be separated easily from solution by an external magnetic field.

3.3. Effect of temperature on the photodegradation of MB under visible-light irradiation

The influence of temperature on the rate constant (k) was also studied. As shown in Fig. 3D, the rate constant (k) increased first and then decreased with rising temperatures. It reached a maximum value at 0.01483 min^{-1} at 25 °C.

3.4. Effect of adsorption on the photodegradation of MB

The preliminary adsorption of MB on the $CoFe_2O_4$-graphene photocatalyst surface is a prerequisite for highly efficient photooxidation [42,43]. Fig. 4A illustrates the MB adsorption isotherm from aqueous solution on the $CoFe_2O_4$-G(0.4) photocatalyst at 20 °C with different initial concentrations of MB (10, 20, 30, 40, 50, 60, 80, 100, 200, 300 mg/L), where the amount of equilibrium adsorption (q_e) is plotted as a function of equilibrium concentration in the bulk solution(c_e) (Eq. (1)). It can be seen that the curve demonstrates Langmuir type behavior due to the monolayer coverage of MB on the surface of $CoFe_2O_4$-G(0.4) and the homogeneous distribution of active sites on the surface.

Fig. 7S displays the remaining solution of MB after reaching the adsorption–desorption equilibrium in the dark with the pure $NiFe_2O_4$, reduced graphene oxide and $CoFe_2O_4$-G(0.4). It was obvious that most dye molecules (ca. 96%) remained in the solution with pure $CoFe_2O_4$ as the catalyst after equilibrium, while a large amount of dye molecules (ca. 75%) was adsorbed on the surface of $CoFe_2O_4$-G(0.4). The enhanced adsorptivity should be largely assigned to the π–π stacking and/or electrostatic attraction between MB and π-conjugation regions of the graphene sheets [9]. For the reduced

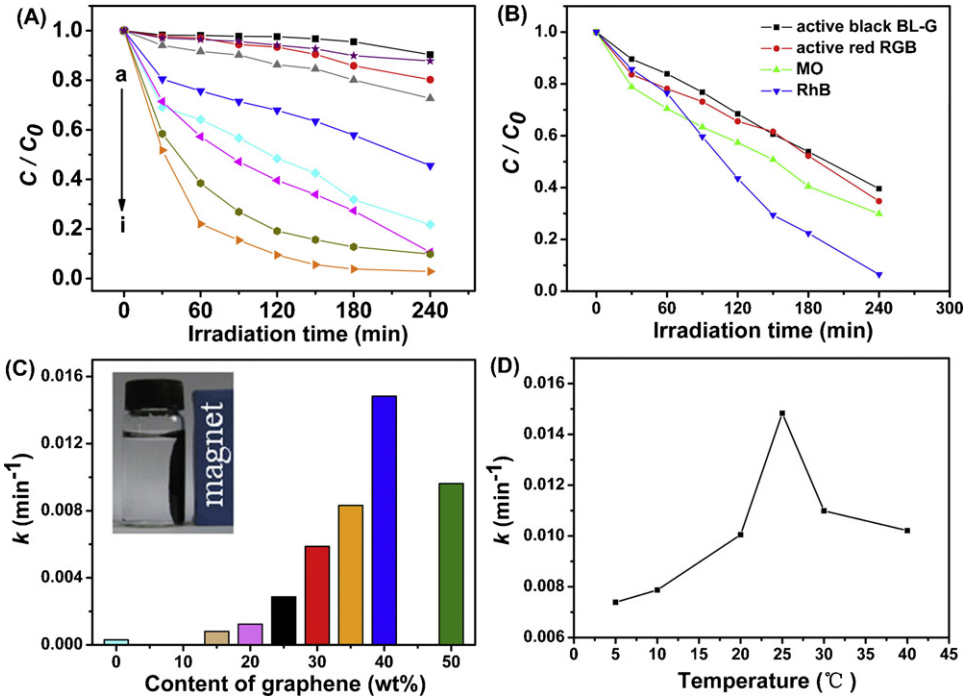

Fig. 3. (A) Effect of different catalysts on photocatalytic degradation of MB: (a) pure $CoFe_2O_4$, (b) $CoFe_2O_4$-G(0.15), (c) $CoFe_2O_4$-G(0.2), (d) $CoFe_2O_4$-G(0.25), (e) $CoFe_2O_4$-G(0.3), (f) $CoFe_2O_4$-G(0.35), (g) $CoFe_2O_4$-G(0.5) and (h) $CoFe_2O_4$-G(0.4); (B) the photodegradation rate of RhB, MO, active black BL-G and active red RGB over $CoFe_2O_4$-G(0.4) under visible-light irradiation; (C) the rate constant for the photodecomposition of MB on $CoFe_2O_4$-graphene photocatalysts with different graphene content. The inset reveals the magnetic separation property of $CoFe_2O_4$-graphene nanocomposite photocatalyst; (D) the rate constant for the photodecomposition of MB on $CoFe_2O_4$-G(0.4) photocatalysts at different temperatures.

graphene oxide, only about 23% of dye molecules was adsorbed, which could be ascribed to the fact that during the solvothermal reduction, deoxygenation of graphene oxide gave rise to layer stacking and formation of aggregates.

The temperature also affects the adsorption of dyes onto solid surfaces. Fig. 4B reveals the relationship between the temperature and the equilibrium adsorption (q_e) on the $CoFe_2O_4$-G(0.4) surface using initial concentration (30 mg/L) of the MB. It can be seen that the trend of variation in q_e is in accordance with that of rate constant (k), namely, rate constant (k) first increased and then decreased with rising temperatures, and it reached a maximum value (85.35 mg/g) at 25 °C.

3.5. Mechanism of photocatalytic activity enhancement

Among the $CoFe_2O_4$-graphene catalysts, $CoFe_2O_4$-G(0.4) showed the highest photocatalytic activity for MB degradation under visible light. The significant enhancement in photoactivity can be attributed to the remarkable synergistic effect of the combination of $CoFe_2O_4$ and the graphene sheets, leading to the efficient separation of photogenerated carriers in the $CoFe_2O_4$ and graphene coupling system. A possible mechanism for the photocatalytic enhancement is proposed as follows and is shown in Fig. 5.

$$CoFe_2O_4 + h\nu \rightarrow CoFe_2O_4(h + e) \quad (1)$$

$$CoFe_2O_4(e) + \text{graphene} \rightarrow CoFe_2O_4 + \text{graphene}(e) \quad (2)$$

$$\text{graphene}(e) + O_2 \rightarrow O_2^{\bullet -} + \text{graphene} \quad (3)$$

$$CoFe_2O_4(h) + OH^- \rightarrow CoFe_2O_4 + {}^{\bullet}OH \quad (4)$$

$$CoFe_2O_4(h) + {}^{\bullet}OH + O_2^{\bullet -} + MB \rightarrow CO_2 + H_2O + SO_4^- + NO_3^- + Cl^- \quad (5)$$

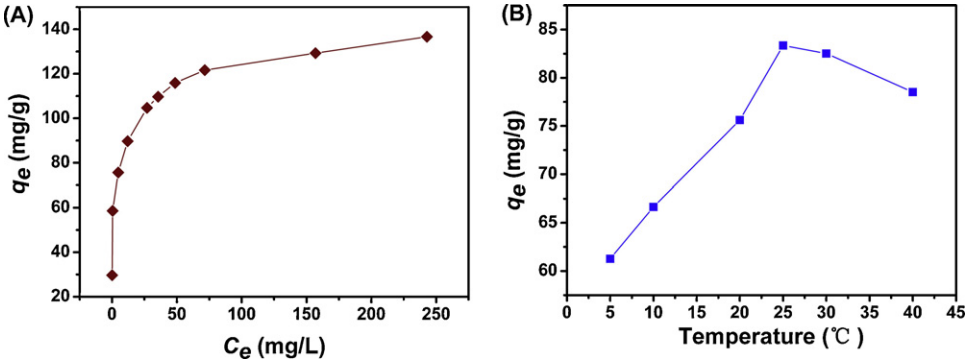

Fig. 4. (A) Adsorption isotherm of MB on the $CoFe_2O_4$-G(0.4) photocatalyst at 20 °C with different initial concentrations of MB (10, 20, 30, 40, 50, 60, 80, 100, 200, 300 mg/L); (B) the values of equilibrium adsorption (q_e) on the $CoFe_2O_4$-G(0.4) surface using initial concentration 30 mg/L of the MB at different temperatures.

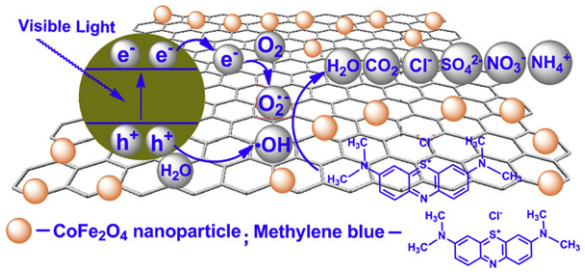

Fig. 5. Proposed mechanism of photocatalytic activity enhancement.

Upon irradiation with visible light, $CoFe_2O_4$ nanoparticles undergo charge separation to yield electrons (e) and holes (h) (reaction (1)). Because graphene sheets are known as good electron acceptors [44], the electrons are quickly transferred to the graphene sheets via a percolation mechanism (reaction (2)). Then the negatively charged graphene sheets can react with the dissolved oxygen to produce superoxide anion radicals (reaction (3)), while the holes are scavenged by the adsorbed water to form hydroxyl radicals (reaction (4)). Finally, the active species (holes, superoxide anion radical and hydroxyl radical) oxidize the MB molecules adsorbed on the active sites of the $CoFe_2O_4$-graphene system through the π–π stacking and/or electrostatic attraction (reaction (5)).

EIS is a powerful nondestructive technique to characterize the electrical conductivity of the catalyst and understand the synergistic effect between $CoFe_2O_4$ and graphene. As shown in Fig. 6A, the impedance plot of $CoFe_2O_4$-G(0.4) has a very small radius, far smaller than those of GO and pure $CoFe_2O_4$ electrodes. A significant decrease in charge transfer resistance of $CoFe_2O_4$-G(0.4) can be largely attributed to the reduction of graphene oxide in the hydrothermal reaction process. The smaller charge-transfer resistance provides the more significant contribution to the large enhancement of photocatalytic activity, since the photogenerated electrons from the $CoFe_2O_4$ nanoparticles can transfer easily from the conduction band to the reduced graphene oxide, leading to the spatial separation of the electron and hole, thereby preventing direct recombination.

To investigate the synergistic effect between nanoparticles and graphene sheets, photocurrent measurements were carried out for pure $CoFe_2O_4$, $ZnFe_2O_4$-G(0.2) and $CoFe_2O_4$-G(0.4) after deposition on ITO electrodes via several on–off cycles of irradiation. Fig. 6B shows the photocurrent transient responses under visible light and darkness for these samples where the photocurrent was measured at 0.0 V vs SCE in 0.5 M Na_2SO_4 aqueous solution. The photocurrent of the $CoFe_2O_4$-G(0.4) electrode (0.125 μA) was about 10 times higher than that of the pure $CoFe_2O_4$ electrode (0.013 μA), indicating that the synergistic effect can significantly improve the separation efficiency of photoinduced electrons and holes. It can also be noted that the $ZnFe_2O_4$-G(0.2) electrode only gave a photocurrent response of 0.05 μA, much smaller than that of $CoFe_2O_4$-G(0.4), and therefore explains why $ZnFe_2O_4$-G(0.2) shows high photocatalytic activity only in the presence of hydrogen peroxide [17]. Generation of the photocurrent from visible light by the excitation of electron–hole pairs on the $CoFe_2O_4$ surface can be explained based on the following proposed mechanism. Under visible-light irradiation, $CoFe_2O_4$ nanoparticles undergo charge separation to yield electrons (e) and holes (h). Because graphene sheets are known as good electron acceptors, the electrons are quickly transferred to the graphene sheets and collected by the ITO electrode to generate photocurrent, while the holes are scavenged by the adsorbed water to form hydroxyl radicals [10,44–48].

The photoluminescence (PL) spectra of the photocatalysts are useful to disclose the migration, transfer, and recombination processes of the photogenerated electron–hole pairs in the semiconductors. Fig. 7A presents PL emission spectra of pure $CoFe_2O_4$ and $CoFe_2O_4$-G(0.4) photocatalyst monitored at an excitation wavelength of 253 nm. It can be seen that the emission of pure $CoFe_2O_4$ is centered at 380 nm, which is attributed to the recombination of holes and electrons in the valence and conduction bands. The $CoFe_2O_4$-G(0.4) heteroarchitecture exhibited a much lower emission intensity than pure $CoFe_2O_4$, implying that the recombination of photogenerated electrons and holes is inhibited greatly in the $CoFe_2O_4$-G(0.4) system. Because of their efficient electron-transport property, graphene sheets can significantly quench the fluorescence from $CoFe_2O_4$ anchored on them. The photogenerated electrons of excited $CoFe_2O_4$ were transferred instantly from the conduction band of $CoFe_2O_4$ to graphene via a percolation mechanism, resulting in an improved and efficient charge separation and consequently exhibiting much higher photocatalytic activity [9,49].

It is important to identify the main active oxidant in the photocatalytic reaction process for understanding the photocatalytic mechanism. The oxidants generated in the photocatalytic process can be measured through trapping by disodium ethylenediamine tetraacetate (EDTA–2Na) and tert-butyl alcohol (t-BuOH) [15]. As shown in Fig. 7B, the addition of t-BuOH greatly reduces the photodegradation rate of MB in the $CoFe_2O_4$-G(0.4) suspension, whereas the addition of EDTA–Na has little effect on the photodegradation rate of MB. These phenomena suggest that most of the photogenerated holes can react with the adsorbed water (or hydroxide anions) to give hydroxyl radicals, and only a few of them can directly oxidize MB molecules. Therefore, we can conclude that hydroxyl radicals play the role of main oxidant in the $CoFe_2O_4$-G(0.4) system and the radical oxidation reaction mechanism predominates.

After photocatalytic reactions on the $CoFe_2O_4$-G(0.4) system were complete, the aqueous solution was analyzed using ion chromatography (Dionex ICS-90). The chromatogram of the solution

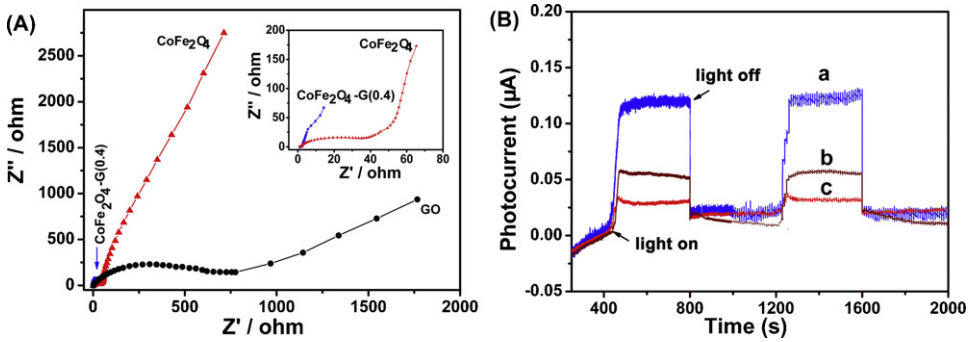

Fig. 6. (A) The electrochemical impedance spectra (EIS) of $CoFe_2O_4$-G(0.4), pure $CoFe_2O_4$ and GO. The spectrum in the inset is enlarged to show the impedance of $CoFe_2O_4$-G(0.4) and pure $CoFe_2O_4$; (B) photocurrent transient responses of (a) $CoFe_2O_4$-G(0.4), (b) $ZnFe_2O_4$-G(0.2) and (c) pure $CoFe_2O_4$ electrodes under visible-light irradiation, $[Na_2SO_4] = 0.5$ M.

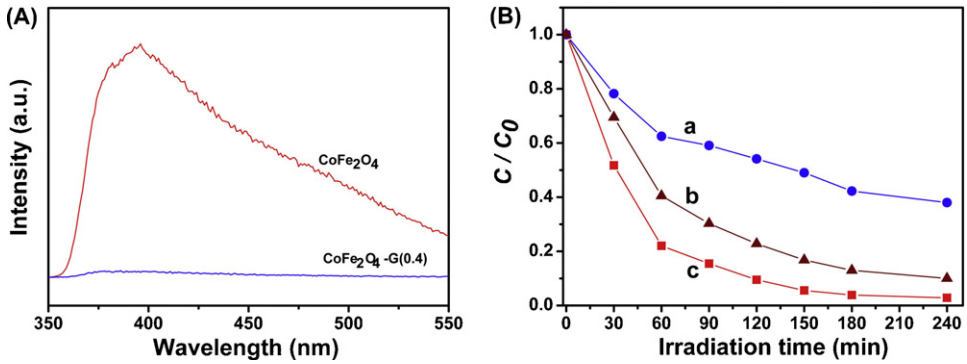

Fig. 7. (A) The room temperature photoluminescence (PL) spectra of pure $CoFe_2O_4$ and $CoFe_2O_4$-G(0.4) (λ_{ex} = 253 nm); (B) photocatalytic degradation of MB under visible-light irradiation at 25 °C with (a) $CoFe_2O_4$-G(0.4) + t-BuOH, (b) $CoFe_2O_4$-G(0.4) + EDTA–Na and (c) $CoFe_2O_4$-G(0.4).

contained three peaks for the SO_4^{2-}, NO_3^-, and Cl^- ions (Fig. 8S). The strongest peak, SO_4^{2-}, implied the sulfur atoms were completely oxidized to SO_4^{2-} ions. The relatively weak signal of NO_3^- indicated that some of the nitrogen atoms were oxidized to NO_3^-. Interestingly, it was reported that NH_4^+ was the only product of nitrogen transformation for photodegradation [50]. The formation of NO_3^- also gave evidence for the strong catalytic oxidation ability of the $CoFe_2O_4$-G(0.4) system.

4. Conclusions

In conclusion, a magnetically separable $CoFe_2O_4$-graphene photocatalyst with differing graphene content has been successfully prepared via a one-step hydrothermal method. TEM observations indicate that graphene sheets are fully exfoliated and decorated with $CoFe_2O_4$ nanocrystals having an average diameter of 5.53 nm and a narrow particle size distribution. The photocatalytic activity measurements demonstrate that the combination of $CoFe_2O_4$ nanoparticles with graphene sheets results in a dramatic conversion of the inert $CoFe_2O_4$ into a highly active catalyst for the degradation of MB, RhB, MO, active black BL-G and active red RGB under visible-light irradiation. The significant enhancement in photoactivity can be ascribed to the reduction of graphene oxide, as the excellent conductivity of the reduced graphene oxide sheets is favorable for the efficient separation of photogenerated carriers in the $CoFe_2O_4$ and graphene coupling system.

Supplementary information

AFM image, XPS data of C 1s, Co 2p and Fe 2p of $CoFe_2O_4$-G(0.4) catalyst; BET data of $CoFe_2O_4$-G(0.4) catalyst; Raman, XRD patterns, UV–vis absorbance spectra of $CoFe_2O_4$-graphene nanocomposites with different graphene content and Ion chromatography analysis of the solution after the photocatalytic reactions on the $CoFe_2O_4$-G(0.4) system.

Acknowledgements

This investigation was supported by the National Natural Science Foundation of China (no. 21171094), the Science and Technology Department of Jiangsu Province (BE2009159, BE2009175), NUST Research Funding (2011PYXM03) and the Department of Education of Jiangsu Province (CXZZ11_0245).

Appendix A. Supplementary data

Supplementary data associated with this article can be found, in the online version, at doi:10.1016/j.apcatb.2011.10.009.

References

[1] W.H. Lee, J. Park, S.H. Sim, S.B. Jo, K.S. Kim, B.H. Hong, K. Cho, Adv. Mater. 23 (2011) 1752–1756.
[2] S. Chen, J. Zhu, X. Wang, ACS Nano 4 (2010) 6212–6218.
[3] S.-E. Zhu, R. Shabani, J. Rho, Y. Kim, B.H. Hong, J.-H. Ahn, H.J. Cho, Nano Lett. 11 (2011) 977–981.
[4] D.R. Wang, G. Ye, X.L. Wang, X.G. Wang, Adv. Mater. 23 (2011) 1122–1125.
[5] A. Cao, Z. Liu, S. Chu, M. Wu, Z. Ye, Z. Cai, Y. Chang, S. Wang, Q. Gong, Y. Liu, Adv. Mater. 22 (2010) 103–106.
[6] C. Xu, X. Wang, J.W. Zhu, X.J. Yang, L.D. Lu, J. Mater. Chem. 18 (2008) 5625–5629.
[7] J.W. Zhu, G.Y. Zeng, F.D. Nie, X.M. Xu, S. Chen, Q.F. Han, X. Wang, Nanoscale 2 (2010) 988–994.
[8] Y.M. Li, X.J. Lv, J. Lu, J.H. Li, J. Phys. Chem. C 114 (2010) 21770–21774.
[9] H. Zhang, X. Lv, Y. Li, Y. Wang, J. Li, ACS Nano 4 (2010) 380–386.
[10] O. Akhavan, ACS Nano 4 (2010) 4174–4180.
[11] G. Williams, B. Seger, P.V. Kamat, ACS Nano 2 (2008) 1487–1491.
[12] Y. Zhang, Z.-R. Tang, X. Fu, Y.-J. Xu, ACS Nano 4 (2010) 7303–7314.
[13] D.H. Yoo, V.C. Tran, V.H. Pham, J.S. Chung, N.T. Khoa, E.J. Kim, S.H. Hahn, Curr. Appl. Phys. 11 (2011) 805–808.
[14] O. Akhavan, Carbon 49 (2011) 11–18.
[15] T.G. Xu, L.W. Zhang, H.Y. Cheng, Y.F. Zhu, Appl. Catal. B 101 (2011) 382–387.
[16] C. Chen, W. Cai, M. Long, B. Zhou, Y. Wu, D. Wu, Y. Feng, ACS Nano 4 (2010) 6425–6432.
[17] Y.S. Fu, X. Wang, Ind. Eng. Chem. Res. 50 (2011) 7210–7217.
[18] S. Shylesh, V. Schunemann, W.R. Thiel, Angew. Chem. Int. Ed. 49 (2010) 3428–3459.
[19] H.B. Na, I.C. Song, T. Hyeon, Adv. Mater. 21 (2009) 2133–2148.
[20] Y. Hou, X.Y. Li, Q.D. Zhao, X. Quan, G.H. Chen, Adv. Funct. Mater. 20 (2010) 2165–2174.
[21] K.-H. Choi, K.-K. Wang, E.P. Shin, S.-L. Oh, J.-S. Jung, H.-K. Kim, Y.-R. Kim, J. Phys. Chem. C 115 (2011) 3212–3219.
[22] H. Zheng, J. Wang, S.E. Lofland, Z. Mohaddes-Ardabili, L. Ma, T. Zhao, L. Salamanca-Riba, S.R. Shinde, S.B. Ogale, F. Bai, D. Viehland, Y. Jia, D.G. Schlom, M. Wuttig, A. Roytburd, R. Ramesh, Science 303 (2004) 661.
[23] K.K. Senapati, C. Borgohain, P. Phukan, J. Mol. Catal. A 339 (2011) 24–31.
[24] H.A.J.L. Mourão, A.R. Malagutti, C. Ribeiro, Appl. Catal. A 382 (2011) 284.
[25] N.W. Li, M.B. Zheng, X.F. Chang, G.B. Ji, H.L. Lu, L.P. Xue, L.J. Pan, J.M. Cao, J. Solid State Chem. 184 (2011) 953–958.
[26] B. Das, B. Choudhury, A. Gomathi, A.K. Manna, S.K. Pati, C.N.R. Rao, Chem. Phys. Chem. 12 (2011) 937–943.
[27] W.S. Hummers, R.E. Offeman, J. Am. Chem. Soc. 80 (1958) 1339.
[28] H. Wang, Q. Hao, X. Yang, L. Lu, X. Wang, ACS Appl. Mater. Interfaces 2 (2010) 821–828.
[29] C. Xu, X. Wang, L. Yang, Y. Wu, J. Solid State Chem. 182 (2009) 2486–2490.
[30] D.R. Dreyer, S. Murali, Y. Zhu, R.S. Ruoff, C.W. Bielawski, J. Mater. Chem. 21 (2011) 3443–3447.
[31] C. Nethravathi, M. Rajamathi, Carbon 46 (2008) 1994–1998.
[32] V.C. Tung, M.J. Allen, Y. Yang, R.B. Kaner, Nat. Nanotechnol. 4 (2009) 25.
[33] S. Stankovich, D.A. Dikin, R.D. Piner, K.A. Kohlhaas, A. Kleinhammes, Y. Jia, Y. Wu, S.T. Nguyen, R.S. Ruoff, Carbon 45 (2007) 1558–1565.
[34] T.N. Lambert, C.A. Chavez, B. Hernandez-Sanchez, P. Lu, N.S. Bell, A. Ambrosini, T. Friedman, T.J. Boyle, D.R. Wheeler, D.L. Huber, J. Phys. Chem. C 113 (2009) 19812–19823.
[35] K.S. Vasu, B. Chakraborty, S. Sampath, A.K. Sood, Solid State Commun. 150 (2010) 1295–1298.
[36] S.C. Ray, A. Saha, S.K. Basiruddin, S.S. Roy, N.R. Jana, Diamond Relat. Mater. 20 (2011) 449–453.
[37] I. Calizo, A.A. Balandin, W. Bao, F. Miao, C.N. Lau, Nano Lett. 7 (2007) 2645–2649.
[38] A.C. Ferrari, J.C. Meyer, V. Scardaci, C. Casiraghi, M. Lazzeri, F. Mauri, S. Piscanec, D. Jiang, K.S. Novoselov, S. Roth, A.K. Geim, Phys. Rev. Lett. 97 (2006) 187401.
[39] L. Li, J. Sol–Gel Sci. Technol. 58 (2011) 677–681.
[40] J. Barbosa, B. Almeida, J.A. Mendes, A.G. Rolo, J.P. Araujo, Phys. Status Solidi A 204 (2007) 1731–1737.

[41] H.L. Yuan, Y.Q. Wang, S.M. Zhou, L.S. Liu, X.L. Chen, S.Y. Lou, R.J. Yuan, Y.M. Hao, N. Li, Nanoscale Res. Lett. 5 (2010) 1817–1821.
[42] N. Bao, Y.A. Li, Z.T. Wei, G.B. Yin, J.J. Niu, J. Phys. Chem. C 115 (2011) 5708–5719.
[43] Y. Xu, C.H. Langford, Langmuir 17 (2001) 897–902.
[44] I.V. Lightcap, T.H. Kosel, P.V. Kamat, Nano Lett. 10 (2010) 577–583.
[45] Y.H. Ng, I.V. Lightcap, K. Goodwin, M. Matsumura, P.V. Kamat, J. Phys. Chem. Lett. 1 (2010) 2222–2227.
[46] Y.H. Ng, A. Iwase, A. Kudo, R. Amal, J. Phys. Chem. Lett. 1 (2010) 2607–2612.
[47] K. Vinodgopa, S. Hotchandani, P.V. Kamat, J. Phys. Chem. 97 (1993) 9040–9044.
[48] K.K. Manga, Y. Zhou, Y.L. Yan, K.P. Loh, Adv. Funct. Mater. 19 (2009) 3638–3643.
[49] X. Wang, L.J. Zhi, K. Mullen, Nano Lett. 8 (2008) 323–327.
[50] Y.J. Wang, R. Shi, J. Lin, Y.F. Zhu, Appl. Catal. B 100 (2010) 179–183.